ChemComm

COMMUNICATION

View Article Online
View Journal

Cite this: DOI: 10.1039/d5cc07127e

Received 16th December 2025,
Accepted 14th January 2026

DOI: 10.1039/d5cc07127e

rsc.li/chemcomm

Plasmonic nanopore to monitor in-pore chemistry

Weihong Wang,[a] Shukun Weng,[b] Ali Douaki,[bc] German Lanzavecchia,[bc] Yanqiu Zou,[d] Qifei Ma,[a] Huaizhou Jin,[e] Roman Krahne,[b] Shangzhong Jin,*[a] Makusu Tsutsui *[f] and Denis Garoli *[abc]

Reliable control of solid-state nanopore gating remains challenging. Voltage-controlled metal phosphate reactions enable reversible pore blocking *via* cyclic precipitation and dissolution driven by cation transport. Negative bias blocks ion flow, while polarity reversal restores conductance, forming a nanofluidic diode. Here we show how plasmonic nanopores allow in-pore SERS measurements, directly confirming the localized chemistry and enabling high-resolution monitoring of nanoscale processes.

Over the past two decades, solid-state nanopore technology has been the focus of extensive research, particularly aimed at creating artificial systems that mimic biological nanopores, *i.e.* transmembrane proteins capable of regulating the passage of individual molecules and ions.[1–4] While the primary effort has traditionally centered on sequencing applications,[5–9] the scope of interest in nanopore systems has now expanded considerably. Among various research directions, the use of solid-state nanopores for constructing nanofluidic circuits, such as ionic transistors and diodes, has recently attracted significant attention.[2,10–12] To develop a nanofluidic ionic system that mimics the behavior of a diode, precise control over the nanopore's geometry and surface charges is essential.[13,14] In this context, a novel strategy for fabricating solid-state nanopores exhibiting diode-like properties, characterized by exceptionally high ion current rectification (ICR), has been recently demonstrated by Tsutsui *et al.*[15] This method relies on the so-called "in-pore chemistry," where two solutions interact at the interface between the *cis* and *trans* reservoirs of the nanopore chamber, an interface effectively defining the nanopore volume itself. In particular, this can be possible by using a thin Si_3N_4 membrane including a nanopore connecting two distinct ionic reactant solutions for precise confinement of the ion electromigration. These ions are capable of inducing electrically tunable metal phosphate precipitation/dissolution in the pore. This can be applied to the preparation of advanced nanofluidic devices including diodes and memristors representing a significant plus with respect to the conventional nano-scale systems.[16–18] A similar method has been more recently reported by Siwy *et al.*, where the cycling precipitation and dissolution inside the nanopore are used to investigate ionic memory effects.[19] To improve our understanding on the reported "in-pore chemistry",[15] here we investigated the chemical reaction inside the nanopore using optical spectroscopy. Considering that the reaction takes place in a very small volume (with a nanopore's diameter of 200 nm and thickness of 50 nm, the volume is of the order of 10^{-3} fL), the chemical reaction can be monitored only using a highly localized label free spectroscopy. In particular, Surface Enhanced Raman Spectroscopy (SERS) represents a valuable technique where the electromagnetic field can be squeezed in the nanopore volume thanks to a proper design of a plasmonic nanopore.[4,20] Therefore, in this work we replaced the Si_3N_4 nanopore previously used[15,21] with a plasmonic nanopore designed as a thin gold layer on a Si_3N_4 membrane where the nanopore is surrounded by a bulls-eye grating with a period matching the excitation of the surface plasmon polaritons at the laser wavelength used for the excitation. As extensively proved in literature,[20,22–28] this structure enables a strong near-field enhancement inside the nanopore, therefore facilitating measurements of the vibrational spectra during the precipitation/dissolution reactions. The bulls-eye integrated plasmonic nanopores were fabricated by means of focused ion beam (FIB) milling in a 50 nm thick Si_3N_4 membrane supported on a Si wafer (See SI for details). An initial pore's diameter of about 200 nm was prepared.[15] The sample was then modified with an

[a] College of Optical and Electronic Technology, China Jiliang University, Hangzhou 310018, China. E-mail: jinsz@cjlu.edu.cn, denis.garoli@unimore.it
[b] Istituto Italiano di Tecnologia, Via Morego 30, 16136, Genova, Italy
[c] Dip. di Scienze e Metodi dell'Ingegneria, Università di Modena e Reggio Emilia, via Amendola 2, 42122, Reggio Emilia, Italy
[d] State Key Laboratory of Modern Optical Instrumentation, College of Optical Science and Engineering, Zhejiang University, Hangzhou 310027, China
[e] Key Laboratory of Quantum Precision Measurement, College of Physics, Zhejiang University of Technology, Hangzhou, China
[f] SANKEN, The University of Osaka, Ibaraki 567-0047, Osaka, Japan. E-mail: makusu32@sanken.osaka-u.ac.jp

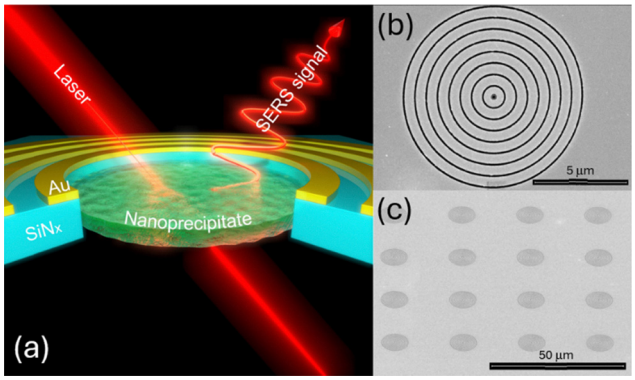

Fig. 1 Concept and fabrication. (a) Schematic illustration of the precipitation/dissolution at the nanopore aperture that can be monitores with SERS; (b) top view of a single plasmonic nanopore with a bulls-eye grating around it; (c) tilted view of an array of bulls-eye/nanopores.

additional thin bilayer of Ti/Au (5/25 nm) and a successive FIB sculpturing was used to prepare a bull-eye grating with a grating period matching the surface plasmon polariton wavelength (λ_{SPP}) for an incident light at 532 nm (see SI for details on the electromagnetic field confinement produced by this structure).[29,30] Fig. 1 shows an illustration of the process and reports SEM images of the fabricated sample.

As a first step we characterize the electrical properties of the nanopore to verify if our design comprising the Ti/Au layers results in the desired diode-like response. Here the metallic layers can, in principle, act as a floating electrode under the external applied field.[31] Therefore, we first measured the current from the nanopore applying a transmembrane voltage (V_b) with a scan rate (r_{scan}) of 60 mV s^{-1} in phosphate-buffered saline containing 1.37 M NaCl at pH 7.4 (hereafter, NaCl solution refers to the PBS unless otherwise denoted). In all our experiments we observed a perfect ohmic behavior with a conductance of 0.5 μS (Fig. 2a), consistent with Maxwell–Hall's model (see SI for details) for d_{pore} of about 200 nm and solution resistivity (ρ_{NaCl}) of 0.08 Ωm. The same set of measurements have been performed replacing PBS respectively with $CaCl_2$ and $MnCl_2$ (concentration 2 mol L^{-1}) on both sides of the microfluidic chamber. These two solutions demonstrated to be very effective in the nanoprecipitation process that will be discussed later. As can be seen from Fig. 2a, also in these cases, symmetric configurations on the *cis* and *trans* sides produce linear ohmic *I–V* response, as also demonstrated in a recent publication by Tsutsui *et al.*[32] The nanopore's conductances were, 0.33 μS and 0.15 μS, respectively for $CaCl_2$ and $MnCl_2$. A completely different response is expected when switching from a symmetric to asymmetric configurations of *cis* and *trans* sides of the chamber. In particular, using PBS at the *trans* side and filling the *cis* compartment with $CaCl_2$ or $MnCl_2$ salts (same concentrations used before) resulted in significant asymmetry in the I_{ion}–V_b characteristics. $CaCl_2$ and $MnCl_2$ exhibited strong suppression of the ionic current at $V_b < 0$. In the case of $CaCl_2$, the rectification ratio ICR = $|I_{max}/I_{min}|$ reached over 20 000 (Fig. 2b), where I_{max} and I_{min} are I_{ion} at V_b = 0.6 V and −0.6 V, respectively. On the contrary, in the case of $MnCl_2$, the ICR reached a value up to 10^5 for a scan rate of 200 mV s^{-1} considering in this second case I_{max} and I_{min} as I_{ion} at V_b = 1 V and −1 V, respectively (see Fig. S1). We note that, in both the cases, relatively small V_b values reach very high ICR values, and consequently, with higher V_b values, the saturation of the current range that can be measured in the nanopore reader was reached (max measurable I = 200 nA). These ICR values are more than an order of magnitude higher than the state-of-the-art systems based on nanofluidic diodes.[33–35] The rectification behavior depends on the voltage scan speed (SI – Fig. S1 and S2). For $CaCl_2$, the maximum rectification is observed at a scan rate of 240 mV s^{-1}, where the ionic current at negative V_b values remains very low and stable, indicating an almost complete suppression of the translocation of high-concentration cations and anions under negative bias. For both $CaCl_2$ and $MnCl_2$, increasing the scan rate markedly diminishes the diode-like response, resulting in lower ICR values (see Fig. S2). Nevertheless, the diode-like behavior can always be recovered by decreasing the scan rate, as shown in Fig. S1. This ionic rectification cannot be justified considering concentration polarization or ion selectivity or electroosmotic flow.[15,32,34,35]

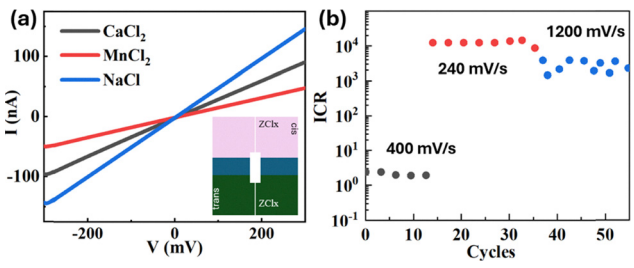

Fig. 2 (a) The ion transport properties under no salt difference (NaCl(blue), $MnCl_2$(red), and $CaCl_2$ (black)). The salinity was also the same at *cis* and *trans*(1.37 M for NaCl and 2 M for the other salts). (b) ICR values obtained for $CaCl_2$ system at different scan rates.

On the contrary, the diode-like behaviour of the nanopore system is due to the formation of a solid precipitate *via* V_b-derived reactions that occluded the space for the electromigration of ions through the pores. Hence, we are observing (a scan rate dependent) precipitation reactions between divalent cations with the phosphoric acid in the electrolyte buffer to form metal phosphates. This can be understood considering the components in our chamber. The main ionic components of PBS in water are: Na^+, Cl^-, HPO_4^{2-} and $H_2PO_4^-$ (the phosphate buffer pair). A divalent chloride compound in aqueous solution dissolves as: XCl_2 (s) → X^{2+} (aq) + $2Cl^-$ (aq), where X represents here Ca and Mn. Calcium and Manganese ions (X^{2+}) are known to react with phosphate ions to form insoluble phosphate salts, with a pH dependent reaction:

$$3X^{2+} + 2PO_4^{3-} \rightarrow X_3(PO_4)_2 \quad (1)$$

In PBS, most phosphate is present as HPO_4^{2-} or $H_2PO_4^-$, but under physiological pH, there is still sufficient PO_4^{3-} to trigger partial precipitation of salts phosphate (especially hydroxyapatite or amorphous X–P compounds). Therefore, the

following reaction most likely happens at the interface between *cis* and *trans* sides:

$$3XCl_2 + 2Na_3PO_4 \rightarrow X_3(PO_4)_2 + 6NaCl \quad (2)$$

This reaction is strongly pH dependent.[15] For this reason the experiments reported here used PBS at physiological pH.

Hence, the electrical response observed in our nanopores is ascribed to a solid-phase precipitate that clogs the aperture of the pore where the two solutions are mixed. The possibility to drive this reaction by external electrical potential is fundamental to provide the diode-like response and the significant ICR values reported. Fig. 3 reports the characterizations performed on the $CaCl_2$ system using the electron microscopy combined with energy dispersion spectroscopy (EDS).

The morphological and compositional characterizations of the nanopore were done at the two stages corresponding to I_{max} and I_{min}, *i.e.* when the external potential was V_b = 0.6 V and −0.6 V, respectively. Fig. 3a and b clearly illustrate what happens inside the nanopore using the plasmonic configuration studied here. Additional tests using bare Si_3N_4 nanopores (reported in SI – note #2), confirmed the precipitation and dissolution reactions. To note, these micrographs can be obtained stopping the reaction at the specific V_b and resulted to be reproducible after multiple cycles. EDS maps revealed the presence of oxygen and phosphor inside the nanopore's cavity, as expected, even if the sensitivity of the technique is probably not enough to obtain convincing results.

We then performed optical spectroscopic analyses by means of Raman spectroscopy. The goal was to obtain the spectrum from the nanopore's cavity in order to monitor the localized chemical reaction. Before to do it, the Raman spectra of the individual compounds were collected preparing them as dry droplet, in the case of PBS (*i.e.* we let the PBS droplet to dry on a solid-state substrate), and as dry powders, in the cases of $CaCl_2$ and $MnCl_2$. Fig. 4a reports the obtained vibration signatures where it is possible to observe how for PBS three peaks dominates, corresponding to 877 cm^{-1}, 979 cm^{-1} and 1077 cm^{-1}, respectively. They are associated with the phosphate (PO_4^{3-}) buffer system, specifically the vibrations of the hydrogen phosphate (HPO_4^{2-}) and dihydrogen phosphate ($H_2PO_4^-$) ions.[36] In the cases of $CaCl_2$ and $MnCl_2$, on the contrary, only a main peak at around 1600 cm^{-1} appeared. This can be associated with the H–O–H bending vibration of the water of crystallization.[37] In the nanopore system we are not dealing with salts powders, but we are interested to monitor the precipitation and dissolution processes driven by the external applied electrical potential. Therefore we also collected the Raman signatures of the precipitated salts as reported in eqn (1). To do that, we mixed the compounds using the same concentrations and pH conditions used in the nanopore experiments and, after letting them dry, we collected the spectra. In both the cases ($Ca_3(PO_4)_2$ and $Mn_3(PO_4)_2$), we can observe the presence of a main peak at around 960 cm^{-1}, clearly corresponding to the vibration of the phosphate group.[38,39] A minor broad peak at around 1600 cm^{-1} can be also detected, as expected, to be associated with the H–O–H bending.[37,40] Having a clear view on the vibrational signatures of the chemicals involved in our reactions, it is possible to proceed with the Raman experiments on the nanopore systems. Considering that this reactions have been firstly demonstrated in a Si_3N_4 pore, we performed the precipitation/dissolution processes focusing the laser over the nanopore directly prepared in a bare Si_3N_4 (the fabrication included both single nanopore and an array of nanopores in order to increase the reaction volume (see SI)). Cycling them applying external electrical potential as discussed

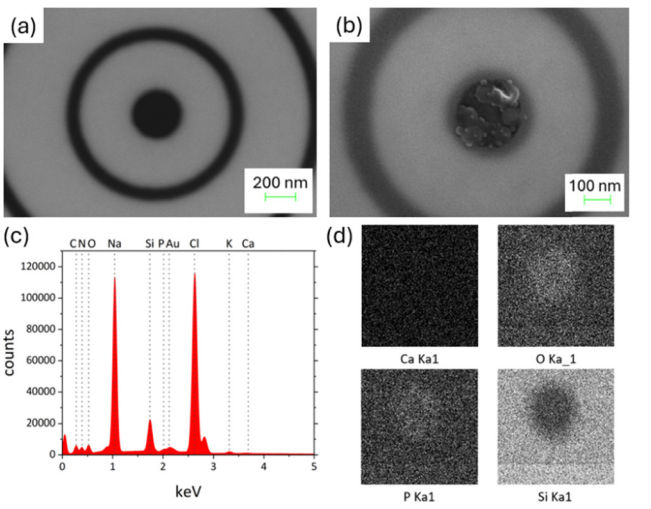

Fig. 3 SEM and EDS of the changes within the nanopore. (a) SEM micrograph of the bare plasmonic pore; (b) $CaCl_2$ precipitate inside the pore; (c) EDS spectrum; (d) EDS maps related to Ca, O, P and Si (additional data in the SI).

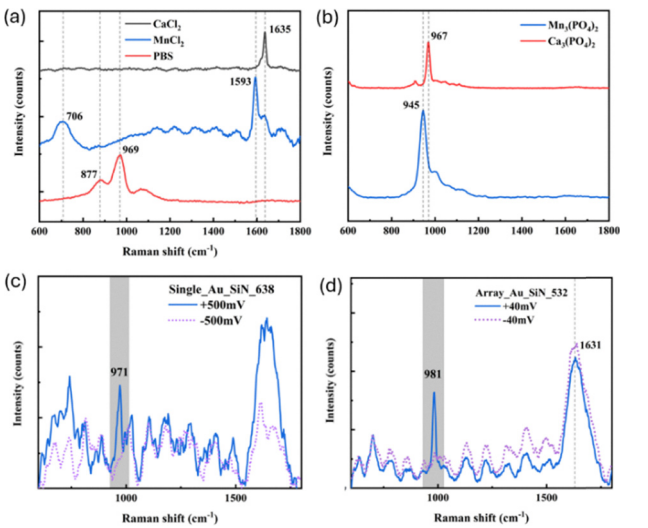

Fig. 4 (a) Raman spectra of powdered samples (PBS(red), $MnCl_2$(blue), and $CaCl_2$(black)). (b) Raman spectra of the precipitate ($Ca_3(PO_4)_2$ (red), $Mn_3(PO_4)_2$ (blue)). (c) Raman spectra of nanopore opening/closing in a Ca-based system (closed (blue), open (purple)). (d) Raman spectra of nanopore opening/closing in a Mn-based system (closed (blue), open (purple)).

above and in ref. 15 we can obtain the precipitation and dissolution processes. Considering the required integration time for the Raman acquisitions (tens of seconds), it was not possible to detect the dynamics of the precipitation reaction. On the contrary, stopping the reaction at V_b = 0.6 V and −0.6 V, we know that the nanopore(s) will be completely open and completely clogged, respectively (as illustrated in SI – Fig. S3). Important to note, the Raman measurements were done using a transparent microfluidic chip compatible with the simultaneous electrical and optical measurements, as demonstrated in ref. 20. This enables the monitoring of the reaction inside the nanopore. In order to avoid the background signal from the PBS solution in the *trans* volume, we excited the pore from the *cis* side where only the chloride salts are present. Testing both a single nanopore and an array of 16 pores it was not possible to detect convincing spectra to be ascribed to the precipitated salts. This is because the volume of detection is spatially limited by the nanopore's diameter. While with the dry precipitates we can collect the signals from large area and large volume samples, here it has not been possible to obtain enough photons from the fL volume of the excited materials. This is the main motivation for the choice of the plasmonic nanopore. In fact, replicating the experiment replacing the bare Si_3N_4 pore with the single plasmonic nanopore (illustrated in Fig. 1b) it was easily possible to collect the SERS signatures from the individual nanopore in the two main configurations (open and clogged) using $CaCl_2$. As can be seen in Fig. 4c, there are clear differences in the Raman spectra associated with open and close pore. In particular, switching from the open to the close configuration, the peak at around 970 cm^{-1} appears, confirming the formation of the phosphate precipitate. While the other spectral regions are not changed, we also observed and increased intensity for the peak at around 1600 cm^{-1}, associated with the H–O–H bending. Performing the same experiment by using $MnCl_2$, it resulted to be more challenging to collect the signatures from a single plasmonic nanopore. Therefore, in order to increase the detection volume, we increased the laser spot size and we explored a configuration comprising 16 nanopores in array (Fig. 1c). In this case, it has been again possible to clearly detect the peak associated to the phosphate salts precipitation, presents only in the spectrum related to the clogged pore, while it always disappeared switching to the open pore configuration.

In conclusion, this study demonstrates the advantages of a plasmonic nanopore platform for probing chemical processes at the nanoscale. By confining intense electromagnetic fields within an attoliter-scale pore, the system enables high spatiotemporal resolution for tracking localized reactions *via* ionic current measurements. Simultaneously, surface-enhanced Raman spectroscopy (SERS) generated at the plasmonic hotspot provides molecular vibrational information, yielding chemical fingerprints of reactants and products. The combination of label-free electrical and optical readouts allows real-time, *in situ* monitoring of dynamic nanoscale processes that are difficult to access using conventional techniques.

Author contributions

W. W. performed the electrical and spectroscopic characterization, S. W., A. D. and G. L. prepared the samples, Y. Z., Q. M. and H. J. supported the data analysis, R. K. provided the access to the lab, S. J., M. T., and D. G. conceived and supervised the work.

Conflicts of interest

There are no conflicts to declare.

Data availability

Data for this article, including SEM micrograph, electrical measurements and Raman spectroscopy data are available on request.

Supplementary information is available. See DOI: https://doi.org/10.1039/d5cc07127e.

Acknowledgements

We are grateful for continued financial support from National Key Research and Development Project of China (No. 2023YFF0613603), National Natural Science Foundation of China (No. 22202167), Provincial Science and Technology Plan Project: Micro and Nano Preparation and Photoelectronic Detection (No. 03014/226063). D. G. thank the HORIZON-MSCADN-2022: DYNAMO, grant Agreement 101072818. A part of this work was supported by the Japan Society for the Promotion of Science (JSPS) KAKENHI Grant Numbers 22H01926, 22H01410, and 24K21715. M. Tsutsui acknowledges support from Kansai Research Foundation for Technology Promotion.

References

1 D. G. Haywood, A. Saha-Shah, L. A. Baker and S. C. Jacobson, *Anal. Chem.*, 2015, **87**, 172–187.
2 S. Zhang, J. Wang, A. Yaroshchuk, Q. Du, P. Xin, M. L. Bruening and F. Xia, *J. Am. Chem. Soc.*, 2024, **146**(16), 11036–11042.
3 E. Angeli, L. Repetto, G. Firpo and U. Valbusa, *Curr. Opin. Electrochem.*, 2021, **29**, 100754.
4 W. Li, J. Zhou, N. Maccaferri, R. Krahne, K. Wang and D. Garoli, *Anal. Chem.*, 2022, **94**, 503–514.
5 Y.-L. Ying, Z.-L. Hu, S. Zhang, Y. Qing, A. Fragasso, G. Maglia, A. Meller, H. Bayley, C. Dekker and Y.-T. Long, *Nat. Nanotechnol.*, 2022, **17**, 1136–1146.
6 T. Zhang, H. Li, M. Jiang, H. Hou, Y. Gao, Y. Li, F. Wang, J. Wang, K. Peng and Y.-X. Liu, *J. Genet. Genomics*, 2024, **51**, 1361–1374.
7 J. Ritmejeris, X. Chen and C. Dekker, *Nat. Rev. Bioeng.*, 2024, **3**, 303–316.
8 A. Dorey and S. Howorka, *Nat. Chem.*, 2024, **16**, 314–334.
9 Z. Zhang, J. Sha, G. Qin, D. Chen, W. Si, Q. Wang and L. Liu, *Small Methods*, 2025, e01603.
10 X. Zhang, Y. Dai, J. Sun, J. Shen, M. Lin and F. Xia, *Anal. Chem.*, 2024, **96**, 2277–2285.
11 B. Yameen, M. Ali, R. Neumann, W. Ensinger, W. Knoll and O. Azzaroni, *J. Am. Chem. Soc.*, 2009, **131**, 2070–2071.
12 G. Pérez-Mitta, J. S. Tuninetti, W. Knoll, C. Trautmann, M. E. Toimil-Molares and O. Azzaroni, *J. Am. Chem. Soc.*, 2015, **137**, 6011–6017.
13 A. J. Storm, J. H. Chen, X. S. Ling, H. W. Zandbergen and C. Dekker, *Nat. Mater.*, 2003, **2**, 537–540.

14 I. Yanagi, T. Ishida, K. Fujisaki and K. Takeda, *Sci. Rep.*, 2015, **5**, 14656.
15 M. Tsutsui, W.-L. Hsu, C. Hsu, D. Garoli, S. Weng, H. Daiguji and T. Kawai, *Nat. Commun.*, 2025, **16**, 1089.
16 P. Ramirez, S. Portillo, J. Cervera, S. Nasir, M. Ali, W. Ensinger and S. Mafe, *J. Chem. Phys.*, 2024, **160**, 044701.
17 J. Cervera, S. Portillo, P. Ramirez and S. Mafe, *Phys. Fluids*, 2024, **36**, 047129.
18 R. Yang, Y. Balogun, S. Ake, D. Baram, W. Brown and G. Wang, *J. Am. Chem. Soc.*, 2024, **146**, 13183–13190.
19 A. D. Cho, A. Wawrzkiewicz-Jałowiecka, C. E. P. Dewi, S. Tang, D. Cain, E. Cao, C. Martens, T. E. Schäffer, J. Cervera, P. Ramirez, S. Mafe and Z. S. Siwy, *J. Am. Chem. Soc.*, 2025, **147**(51), 47559–47572.
20 A. Douaki, S. Weng, G. Lanzavecchia, A. Sapunova, A. Stuber, G. Nanni, N. Nakatsuka, M. Tsutsui, K. Yokota, R. Krahne and D. Garoli, *Adv. Opt. Mater.*, 2025, **13**, 2402189.
21 M. Tsutsui, W. L. Hsu, D. Garoli, A. Douaki, Y. Komoto, H. Daiguji and T. Kawai, *Nat. Commun.*, 2026, in press.
22 G. W. Kim, J.-H. Ko, D. J. Park, S. S. Choi, H. Kim and S. B. Choi, *J. Korean Phys. Soc.*, 2018, **73**, 1698–1702.
23 T. Mahinroosta and S. M. Hamidi, *Appl. Phys. A: Mater. Sci. Process.*, 2022, **128**, 1043.
24 D. Komisar, S. Kumar, Y. Kan, C. Wu and S. I. Bozhevolnyi, *ACS Photonics*, 2021, **8**, 2190–2196.
25 P. Zilio, G. Parisi, D. Garoli, M. Carli and F. Romanato, *Opt. Lett.*, 2014, **39**, 4899.
26 C. R. Crick, P. Albella, H.-J. Kim, A. P. Ivanov, K.-B. Kim, S. A. Maier and J. B. Edel, *ACS Photonics*, 2017, **4**, 2835–2842.
27 J. D. Spitzberg, A. Zrehen, X. F. Van Kooten and A. Meller, *Adv. Mater.*, 2019, **31**, 1900422.
28 C. R. Crick, P. Albella, B. Ng, A. P. Ivanov, T. Roschuk, M. P. Cecchini, F. Bresme, S. A. Maier and J. B. Edel, *Nano Lett.*, 2015, **15**, 553–559.
29 T. Nagasue, T. Shinohara, S. Hasegawa, K. Imura and K. Tawa, *Opt. Express*, 2022, **30**, 7526.
30 A. Ghaffari, S. Kashani, J. Li, P. Gkoupidenis, R. Riehn and Q. Gu, *ACS Nanosci. Au*, 2025, **5**, 306–313.
31 C. Yang, P. Hinkle, J. Menestrina, I. V. Vlassiouk and Z. S. Siwy, *J. Phys. Chem. Lett.*, 2016, **7**, 4152–4158.
32 M. Tsutsui, K. Yokota, W.-L. Hsu, Y. Komoto, D. Garoli, H. Daiguji and T. Kawai, *ACS Nano*, 2025, **19**(48), 41076–41085.
33 Q. Liu, Y. Liu, B. Lu, Y. Wang, Y. Xu, J. Zhai and X. Fan, *RSC Adv.*, 2020, **10**, 7377–7383.
34 H. Daiguji, Y. Oka and K. Shirono, *Nano Lett.*, 2005, **5**, 2274–2280.
35 E. C. Yusko, R. An and M. Mayer, *ACS Nano*, 2010, **4**, 477–487.
36 M. D. Fontana, K. Ben Mabrouk and T. H. Kauffmann, in *Spectroscopic Properties of Inorganic and Organometallic Compounds*, ed. J. Yarwood, R. Douthwaite and S. Duckett, Royal Society of Chemistry, Cambridge, 2013, vol. 44, pp. 40–67.
37 L. M. Uriarte, J. Dubessy, P. Boulet, V. G. Baonza, I. Bihannic and P. Robert, *J. Raman Spectroscopy*, 2015, **46**, 822–828.
38 S. Zhai, X. Wu and E. Ito, *J. Raman Spectroscopy*, 2010, **41**, 1011–1013.
39 P. N. De Aza, C. Santos, A. Pazo, S. De Aza, R. Cuscó and L. Artús, *Chem. Mater.*, 1997, **9**, 912–915.
40 S. Quillard, C. Mellier, R. Gildenhaar, J. Hervelin, P. Deniard, G. Berger and J. M. Bouler, *Key Eng. Mater.*, 2011, **493–494**, 225–230.